

Elemental Distribution in Catalyst-Coated Membranes of Proton Exchange Membrane Water Electrolysers Tracked by Synchrotron X-Ray Fluorescence

Alexander Rex, Leonardo Almeida De Campos, Torben Gottschalk, Dario Ferreira Sanchez, Patrick Trinke, Steffen Czioska, Erisa Saraçi, Boris Bensmann,* Jan-Dierk Grunwaldt, Richard Hanke-Rauschenbach, and Thomas L. Sheppard*

The stability of catalyst layers and membranes in proton exchange membrane water electrolysis (PEMWE) cells represents an ongoing challenge, compounded by the dissolution of components and migration of elements within the catalyst-coated membrane (CCM). Conventional microscopy methods often struggle to efficiently evaluate large cross-sections of PEMWE membranes, which is essential for representative analysis of technical scale CCMs. Herein, synchrotron radiation-based X-Ray fluorescence microscopy is exploited to analyze the stability of CCMs with around 1 μm resolution and a field of view of $\approx 200 \times 75 \mu\text{m}^2$. Three application scenarios are investigated: 1) migration of catalyst elements, 2) dissolution of components, and 3) contaminated water supply containing Fe^{2+} ions. XRF is performed at three different X-Ray energies (11.7, 11.4, and 11.0 keV), revealing the local elemental composition, including Pt, Ir, Ti, and Fe, under different stressing conditions. Notable observations include the distribution of Ir across the membrane and in the cathode catalyst layer, localization of Pt within the membrane, accumulation of Ti in the cathode catalyst layer, and minimal presence of Fe. XRF has been demonstrated to be a powerful analytical tool for accurate and high throughput imaging of catalyst degradation in PEMWE scenarios, particularly of technical scale devices.


1. Introduction

Proton exchange membrane water electrolysis (PEMWE) is emerging as a pivotal technology in green hydrogen production, offering a renewable solution for energy storage and transport. PEMWE distinguishes itself from other hydrogen production

technologies such as alkaline water electrolysis and solid oxide water electrolysis through its rapid response capability, high gas purity under differential pressure, robustness under various operating conditions, and compactness.^[1,2] Both the hydrogen evolution reaction and the oxygen evolution reaction (OER) are catalyzed by noble metals, Pt- and Ir-based catalysts, respectively. While both show excellent performance, the cost and scarcity of such platinum group metals are a significant concern. Despite the rigorous search for more sustainable alternatives, replacing Ir for OER in particular remains a challenge. The commercial viability of PEMWE therefore depends on addressing the long-term stability and activity of the system, which is a critical factor for its widespread adoption. This includes improving the durability of catalyst layers and proton conducting membranes, which control the efficiency of the key reactions.^[3-5]

While PEMWE systems are currently rather widely investigated, persistent challenges exist regarding the stability of catalyst layers and membranes.^[6,7] Of particular importance are the processes and effects of component dissolution and element migration on the catalyst-coated membrane (CCM), including both cell-specific elements and introduced impurities. The Ir-based catalyst is known to be unstable, resulting in migration into

A. Rex, T. Gottschalk, P. Trinke, B. Bensmann, R. Hanke-Rauschenbach
Institute of Electric Power Systems
Leibniz University Hannover
30167 Hannover, Germany
E-mail: boris.bensmann@ifes.uni-hannover.de

 The ORCID identification number(s) for the author(s) of this article can be found under <https://doi.org/10.1002/aesr.202400048>.

© 2024 The Author(s). Advanced Energy and Sustainability Research published by Wiley-VCH GmbH. This is an open access article under the terms of the Creative Commons Attribution License, which permits use, distribution and reproduction in any medium, provided the original work is properly cited.

DOI: 10.1002/aesr.202400048

L. Almeida De Campos, S. Czioska, E. Saraçi, J.-D. Grunwaldt, T. L. Sheppard
Institute for Chemical Technology and Polymer Chemistry
Karlsruhe Institute of Technology
76131 Karlsruhe, Germany
E-mail: thomas.sheppard@kit.edu

D. Ferreira Sanchez
Swiss Light Source
Paul Scherrer Institut
CH-5232 Villigen PSI, Switzerland

E. Saraçi, J.-D. Grunwaldt
Institute of Catalysis Research and Technology
Karlsruhe Institute of Technology
76344 Eggenstein-Leopoldshafen, Germany

the membrane,^[8–10] as well as redeposition within the cathodic catalyst layer,^[11–13] although the dissolution mechanisms of different Ir-based catalyst materials also vary.^[14] Currently, these processes are not sufficiently understood to define effective mitigation strategies. Research by Milosevic et al.^[11] revealed that in a single full-cell test with an accelerated stress test phases at 60 °C, a substantial portion of dissolved Ir from iridium oxide (IrO_x) catalyst accumulates in the cathode (50%) and within the membrane (43%), with minor amounts detected along the anode water line (6%) and cathode water line (1%). This migration pattern suggests not only a loss of valuable catalyst material but also potential impacts on the CCM integrity and the overall efficiency of the PEMWE cell over time. Furthermore, Pt dissolution and its subsequent migration into the membrane have also been observed.^[12,13] In a detailed study by Yu et al. using IrO_x nanoparticles as anode catalyst material,^[12] the formation of Pt–Ir precipitates within the membrane half closest to the cathode was discovered, indicating recombination of dissolved Pt and Ir. This resulted in 11% of the total Pt amount being found within the membrane by the end of testing. Grigoriev et al.^[13] also noted Pt migration into the membrane, manifested as a distinct Pt band near the cathode catalyst layer. Moreover, the dissolution and migration of Ti from an uncoated Ti porous transport layer (PTL) of the anode side suggests migration of Ti through the anodic catalyst layer and membrane, finally enriching the cathodic catalyst layer.^[15–17] In addition, contaminants introduced via feed water, either from inadequate water treatment or from dissolution of stainless steel tubing, have been shown to significantly affect the stability of CCMs.^[18]

To address the challenges of PEMWE systems stability, particularly with respect to the catalyst layer and membrane integrity, high-resolution imaging and sophisticated elemental and structural analyses such as transmission electron microscopy (TEM) are often employed. This can reveal the intricate structural changes and degradation patterns in catalyst layers.^[8,12,13] Although providing a high level of detail, TEM is often limited in detecting dissolved ions and can cause radiation-induced sample damage that could obscure the true extent of degradation.^[8,11] TEM coupled with energy dispersive X-Ray spectroscopy (EDXS) can provide important data on the elemental composition of PEMWE cells, by identifying the distribution of Ir and Pt for example.^[11–13] In spite of that, EDXS struggles to accurately quantify low concentrations of dissolved elements and is furthermore time consuming and can be damaging to the sample.^[8] Scanning electron microscopy (SEM) is often used to analyze surface morphology or cross-sections, providing insights into the morphological changes caused by operational stress.^[11,13,15–17] However, SEM has limited capabilities to quantitatively analyze element redeposition, a gap that necessitates the integration of techniques like inductively coupled plasma mass spectrometry for comprehensive quantitative analysis.^[11] Moreover, complementary techniques such as X-Ray diffraction and X-Ray photoelectron spectroscopy can provide additional insights into the crystalline structure of catalysts and the chemical states of cell components.^[9,10] Nonetheless, these techniques may not fully capture the dynamics of elemental migration and redistribution

processes. Becker et al.^[18] reviewed numerous characterization techniques and their applications in the study of CCMs. The collective limitations of these methodologies, including challenges in accurately quantifying elemental redistribution and detecting dissolved ions, highlight the need for more comprehensive analytical techniques.

Based on the current state of research methods, there is a need for spatially-resolved measurements offering high resolution and elemental sensitivity, especially for studying technical systems like CCMs or other composite catalytic materials. X-Ray fluorescence (XRF) microscopy in principle can offer these characteristics. However, the capabilities of even modern benchtop XRF devices are essentially limited by photon flux. In contrast, XRF performed at synchrotron radiation sources can surpass laboratory instruments by offering significantly higher photon flux.^[19] In turn, this enables the use of strong focusing optics for high-resolution micro- or nanobeam imaging, faster measurement speeds, and improved sensitivity at the synchrotron.^[20] As a result, synchrotron XRF not only facilitates high-quality measurements but also enables studies like metal migration effects of highly dilute species. The latter point is particularly relevant for the study of technical systems such as MEAs or other composite catalytic materials.^[21] In this context, synchrotron radiation-based XRF constitutes a powerful tool for evaluating systems such as PEMWE CCMs. Literature studies have shown the possibility of resolving 2D and 3D maps of element distribution along samples to explore contamination in catalytic systems (e.g., fluid catalytic cracking particles) and degradation or migration of main components.^[22–24] By exploiting high-intensity X-rays at the synchrotron, XRF mapping can be performed relatively rapidly over large (i.e., mm scale) samples while maintaining excellent spatial resolution (i.e., μm scale) and elemental sensitivity. The high sensitivity of XRF imaging typically allows the detection of trace elements at or even below ppm level, as demonstrated in geoscience and aerosol science.^[25,26] This sensitivity is particularly relevant in electrochemistry when dealing with relatively dilute metal systems such as in PEMWE devices. In this regard, the application of XRF to monitor elemental migration and distribution in CCMs for water electrolysis is a promising concept that has rarely been explored in literature.

The aim of this work is to explore 2D XRF mapping for the detection and visualization of the elemental distribution within PEMWE CCM cross-sections. The potential of XRF is explored regarding the observation of elemental distribution across the membrane area, particularly in the Nafion polymeric region. The effectiveness of XRF is therefore validated in terms of assessing key stability issues encountered in PEMWE systems. These issues include evaluating the relative distribution of catalyst elements (Ir, Pt) within the membrane, analyzing the dissolution of PEMWE components (Ti), and investigating the impact of contaminated water supply (Fe). Through these investigations, this research aims to demonstrate a rarely explored approach to gain valuable insights into the performance and stability of PEMWE membranes, particularly of nonmodel systems. This may contribute to our understanding of operational stability in renewable energy technologies.

2. Experimental Section

2.1. Material Under Investigation

This study focuses on commercially available Nafion 115 CCMs from HIAT gGmbH, Germany, characterized by anode and cathode loadings of 2.0 mg cm^{-2} Ir black and 1.0 mg cm^{-2} Pt/C, respectively, and a dry thickness of 0.125 mm . Here, the CCMs were integrated into a single-cell setup and exposed to different stress conditions for analysis. The preparation of the CCMs involved several steps. Before assembly, the CCMs were soaked in deionized water ($\geq 18 \text{ M}\Omega \text{ cm}$) for an hour at room temperature to ensure complete hydration. The anode PTL consisted of sintered titanium fibers (1 mm , 2GDL40–1.00, NV Bekaert SA, Belgium), and the cathode PTL was made of carbon paper (H2312, Freudenberg SE, Germany). These components, along with the CCM, were assembled into a Fraunhofer ISE cell with an active area of 4 cm^2 ,^[27] applying a compression force of 2.5 kN (see Figure S1, Supporting Information). The cells were then installed in the respective test benches and deionized water ($\geq 10 \text{ M}\Omega \text{ cm}$) was supplied at a rate of 80 mL min^{-1} at 80°C on the anode side. The compression force was subsequently increased to 3.0 kN and readjusted after 15 min to compensate for initial settling.

2.2. Stressing Conditions

Two custom-built test benches were used for the experiments: one was for the test runs without added impurities (potentiostat: BCS-815, Biologic, France), while the other was used for the test with Fe^{2+} -contaminants (potentiostat: Zenium X, PP242, Zahner-Elektrik GmbH & Co. KG, Germany). A key aspect of the study was the use of CCMs in three distinct stress conditions. The first type, referred to as “Pristine CCM” involved only mechanical and flooding stresses without any electrical load. This served as a baseline for comparison with other CCMs. The second type, referred to as “100 h CV CCM,” was stressed with constant voltage phases set at 2 V . The total test duration was 137 h , including the conditioning phase and characterization

phases (see Figure S2, Supporting Information). The third type, “ Fe^{2+} -contaminated CCM,” was stressed with an added Fe^{2+} impurity in addition to the predominant constant voltage phases of 2 V . In this experiment, 1 mL of a 260 ppm Fe^{2+} solution containing SO_4^{2-} as counter ions was added to the system’s water volume of 260 mL , resulting in an approximate concentration of 1 ppm Fe^{2+} within the system. Throughout the test, which ran 407 h , including the conditioning phase and characterization phases, the system water volume was recirculated and kept constant at 260 mL (see Figure S3, Supporting Information). The anodic water circuit maintained a constant water volume by monitoring the tank level with a capacitive sensor. If a drop in level occurred, such as due to OER consumption, a linked peristaltic pump replenished the deionized water in the tank, ensuring a constant volume of water during the reaction. An overview of further parameters of the tests is included in Table S1, Supporting Information, and the corresponding electrochemical data are presented in Section S2, Supporting Information.

2.3. Sample Preparation for XRF Mapping

After testing, the CCMs of different load types were removed from the PEMWE single cells and dried in a vacuum oven at 40°C for 12 h . For further processing, a stripe from the center of each CCM was cut out with a scalpel (size: $\approx 3 \text{ mm} \times 5 \text{ mm}$) and embedded in epoxy resin (Figure 1). The 100 h CV CCM used epoxy resin type 1 (Epoxy systems Araldit G 2 cast resin and H 2 hardener, Carl Roth GmbH + Co. KG, Germany), while the Pristine CCM and Fe^{2+} -contaminated CCM samples used epoxy resin type 2 (EMbed 812, Electron Microscopy Sciences, United States). The reason for the different types is that the samples were embedded in resin at different times in two different laboratories. The samples were then cured at 60°C for 38 h in an oven. A quality control step was introduced before further processing, employing optical microscopy (DVM6 Digital Microscope, Leica Mikrosysteme Vertrieb GmbH, Germany) evaluation to identify and exclude any damaged or compromised samples. Only those passing this evaluation

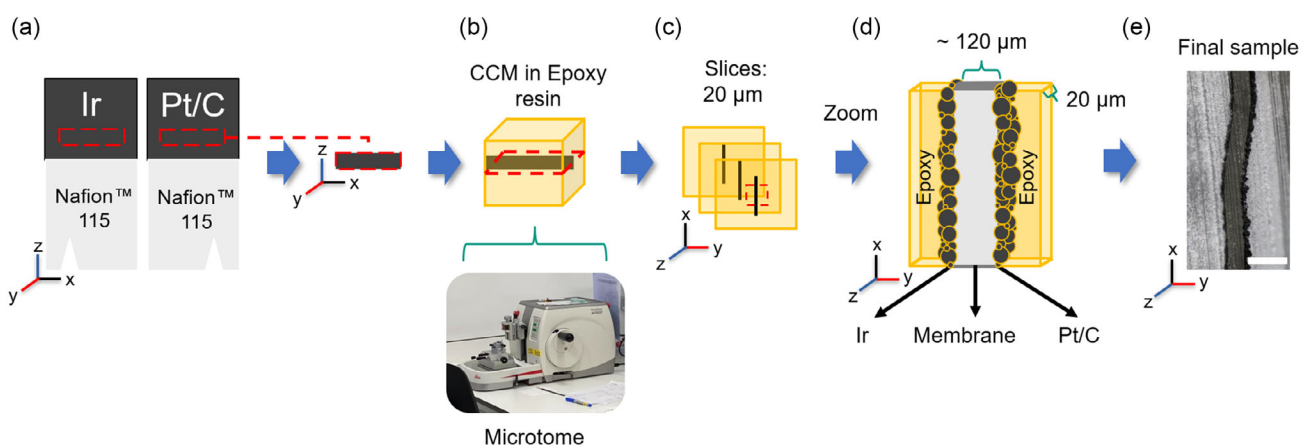


Figure 1. a) Sample preparation for XRF measurements illustrating original form of the disassembled CCMs; b) embedding in epoxy resin and cross-sectioning slicing using a microtome; c) preparation of cross-section series; d) illustration of a single cross-section; and e) final cross-section after cut followed by orientation of the sample system— $200 \mu\text{m}$ scale bar.

proceeded to the next steps. The epoxy resin-fixed samples were individually mounted on supports, followed by precise slicing with a rotating microtome (for 100 h CV CCM: Thermo Scientific HM 340 E Electronic Rotary Microtome, Fisher Scientific GmbH, Germany, and for Pristine CCMs and Fe²⁺-contaminated CCM: HistoCore AUTOCUT-Automated Rotary Microtome, Leica Mikrosysteme Vertrieb GmbH, Germany), producing sections of 20 μm thickness. The samples were then fixed in the sample holder in such a way that the CCM was as close and parallel to the edge of the sample holder as possible so that the CCM had as uniform a vertical and horizontal alignment as possible (see Figure S7, Supporting Information). Subsequently, these prepared samples underwent XRF measurements at microXAS beamline of the Swiss Light Source (SLS) as described in the following sections.

2.4. 2D XRF Mapping

Analysis of elemental distribution in the PEMWE membrane cross-sections was performed by synchrotron-based scanning XRF at the microXAS beamline (SLS, Switzerland), using X-Ray energies of 11.0, 11.4, and 11.7 keV. The beam was focused to a 1 μm spot size with a Kirkpatrick–Baez (KB) mirror system. Four XRF single-element silicon drift detectors (Ketek GmbH, Germany) coupled to FalconX pulse processors (XIA LLC, USA) were positioned around the sample (see Figure S8, Supporting Information). The exit apertures of the collimator detectors were placed at about 10 mm from the sample, with the beryllium (Be) detector windows around 10 mm from the exit aperture of the detector collimators. The volumes between the Be windows and the collimator apertures were constantly flushed with a gentle flow of Helium to minimize absorption of lower energy emission signals (e.g., S, Ti) from the sample. Absorption contrast was recorded simultaneously, by measuring the induced current of the transmitted beam on a 10 μm thick silicon carbide (SiC) diode (incoming intensity, I_0) positioned at the exit of the KB mirrors, and on a 10 μm thick SiC diode (transmitted intensity, I) placed on a beamstop downstream of the sample position. XRF and transmission signals were recorded simultaneously by scanning the sample (up to

≈200 μm × 75 μm) in fly mode, while acquiring measurements at 1 μm intervals using a detector dwell time of 100 ms.

The two catalyst layers composed of Ir and Pt contain relatively high at% content (anode loading: 2.0 mg cm⁻² Ir black, cathode loading: 1.0 mg cm⁻² Pt/C) of either Pt or Ir. To minimize the strong emission signal from Pt and Ir in the electrode layers, which could potentially mask low-intensity signals from elements with orders of magnitude lower at% content in the polymer membrane, a pinhole of 10 μm of diameter was placed at 10 mm from the sample. This aimed to minimize the effects from low-intensity tailings of the beam (i.e., beyond the focused 1 μm spot size) and allow sharper spatial deconvolution of signals. Furthermore, samples were analyzed at three different energies: above absorption L₃ edges of both Pt and Ir (11.7 keV), above L₃ of Ir and below L₃ edge of Pt (11.3 keV), and below both L₃ absorption edges (11.0 keV, see Figure S9, Supporting Information). This was done to effectively deconvolute overlapping signals of Pt and Ir in the polymer membrane, in the event of both species being present. Furthermore, this served as an additional safety measure to confirm that intense fluorescence signals from the electrode layers were effectively excluded from the polymer region.

Following measurements, XRF data were fitted using Python-based scripts and PyMCA libraries.^[28] Each detector was considered independently, and the fitted results were later summed up to generate XRF maps for each sample cross-section (see Figure 2). Finally, two approaches were followed to interpret and evaluate the data: Approach 1) element-specific distribution across the sample cross-section and approach 2) the migration extent and distribution within the membrane. These aspects required distinct methodological approaches, which are described in the following sections.

2.5. XRF Analysis Approach 1: Average Distribution Across the Cross-Section

The initial challenge in analyzing element-specific distribution across the membrane cross-section is separating the membrane area from the catalyst layers. This task is not straightforward due to the gradual and indistinct transition in intensity values

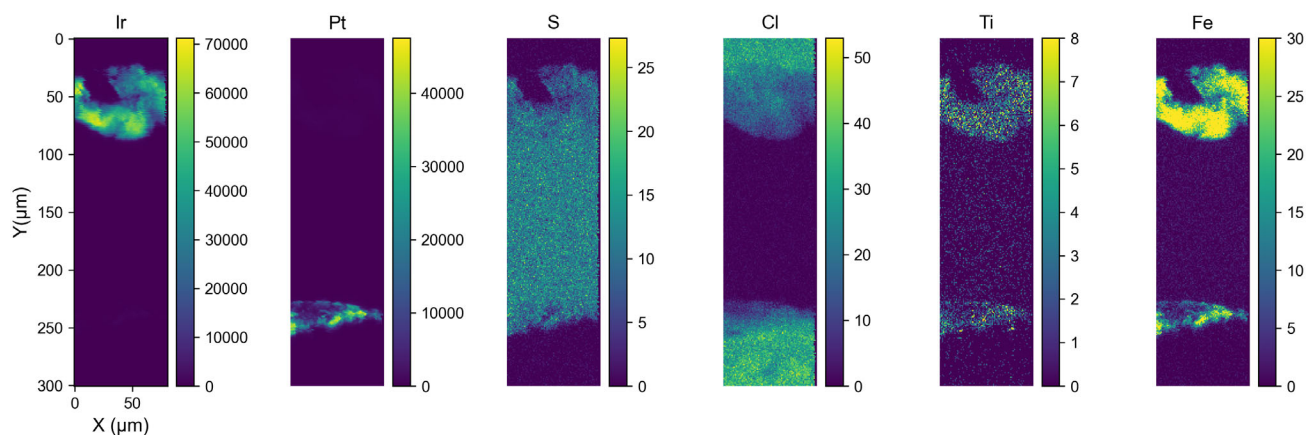


Figure 2. Elemental maps of the pristine sample at 11.7 keV for Ir ($L\beta_1$, $L\beta_2$), Pt ($L\beta_1$, $L\beta_2$), S ($K\alpha$, $K\beta$), Cl ($K\alpha$, $K\beta$), Ti ($K\alpha$, $K\beta$), and Fe ($K\alpha$, $K\beta$) emission signals, with intensity scale indicating detector counts for each signal.

between the catalyst layers, marked by Ir and Pt elements, and the membrane. To address this challenge, the signal of another analyzed element, chlorine (Cl), was utilized to separate the CCM layers (see Figure S10a, Supporting Information). Cl is typically not used in the CCM manufacturing process, and its presence in the system during operation is expected to be minimal. However, the epoxy resins used in sample preparation contain chlorine. Assuming that the liquid epoxy resin partially envelops catalyst particles during embedding, but does not penetrate the polymer membrane, a distinction between the catalyst layers and the membrane can be achieved.

Python was used for subsequent analysis of the CCM. The procedure involves dividing the 2D elemental sample maps provided by earlier evaluation steps into pixel rows, each 1 μm in height and extending across the breadth of the analyzed sample segment. These rows, aligned in a continuous plane, serve as the basis for calculating the average element intensity values, which were then analyzed across the cross-section of the sample. The exact alignment of the pixel rows was achieved through regression analysis of the 2D Cl maps, as detailed in Section S5.1, Supporting Information.

The Cl signal was utilized to define the interface between the membrane and catalyst layers, as outlined in Section S5.2, Supporting Information. However, to accurately assess elemental migration within the membrane cross-section, a critical adjustment was made: the outermost 10-pixel rows adjacent to the catalyst layers were excluded. This exclusion is necessary to avoid potential signal extension beyond the actual membrane area, which could be caused by the tailing of the X-Ray beam during measurement (see Section 2.4). Signals from Ir and Pt, particularly in membrane areas close to the catalyst layer, were thus treated with added caution to avoid possible overlap. Additionally, the physical form of the CCM, especially the degree of curvature and the alignment of the layers, significantly influences how the average intensity values rise toward the catalyst layer. A CCM with a more horizontal orientation and parallel layers exhibits a more pronounced increase in the average intensity values of the pixel rows for Ir and Pt signals, compared to a CCM with significant curvature. This variation in the CCM's physical form impacts the interpretation of elemental distribution within the membrane. These defined orientations and boundaries of the pixel rows (see Figure S10e, Supporting Information) were then extrapolated to the analysis of all other elemental distributions within the sample (see Figure 3a). With these boundaries and orientations of pixel rows established, it was possible to accurately determine the average distribution of the elements along the cross-section of the complete sample (see Figure 3b) and central membrane region (see Figure 3c).

To account for the varying heights of the CCMs, the samples for subsequent analyses were normalized differently depending on the area being analyzed. For the cross-section analysis of the entire sample, normalization occurred with respect to the complete membrane height. When analyzing the central region of the membrane, normalization was specific to this central area. The standard deviation serves as a key analytical parameter for the comparison of element distributions; further details can be found in Section S5.3, Supporting Information. In the presentation of the results, the regions containing twice the standard

deviation (95% confidence interval) are highlighted to illustrate the variation in elemental distribution.

2.6. XRF Analysis Approach 2: Migration Extent and Distribution Within the Membrane

An alternative methodology based on image segmentation was used to assess the extent of metal migration and elemental distribution within the Nafion membrane. This method involved defining intensity thresholds for Pt- and Ir-signals, followed by image segmentation to isolate regions of interest based on the observed emission signal for each element.

Using Python, slices from image stacks were chosen to capture the Pt and Ir XRF emission signals from samples measured at 11.7 keV. Initially, a Gaussian blur ($\sigma = 0.8$) was applied to mitigate measurement noise. Each of the two selected images was subsequently divided into two parts, therefore generating two images with each one containing a catalyst layer signal, one for Ir and another Pt. To acquire the Pt catalyst layer, the top portion of the material was segmented using a threshold set at 100 a.u. for grayscale intensity values. Conversely, for the Ir catalyst layer acquisition, the bottom part of the material was segmented with a threshold of 500 a.u. for grayscale intensity values, as shown in Figure S11a, Supporting Information. Following the segmentation of each catalyst layer, the coordinates of these layers were used to generate two binary masks. One mask contained the excess layer (Binary mask Nafion), encompassing the Nafion membrane and epoxy layers on the external parts of the samples, while the second mask contained both catalyst layers (Binary mask cat.), Figure S11b, Supporting Information. Using the binary mask with coordinates for the Nafion membrane and epoxy layers, a segmented image was created. To eliminate the epoxy layer, the void between the Nafion membrane and epoxy layers was utilized as reference since its signal was defined as zero intensity after thresholding, see Figure S11c, Supporting Information.

For each column (with size defined as 1 pixel) of the image containing Nafion and epoxy, the edges of Nafion layer were segmented by detecting the first zero value after the top epoxy portion and the first zero value after the Nafion layer (bottom region). Every signal before the first zero value and after the first zero after the Nafion layer was transformed into a null signal. This effectively created a mask for only the Nafion membrane. Next, 10 pixels were removed from the top and bottom of the masked membrane, to avoid erroneous signals from beam tailings as discussed previously. A multi-Otsu automated threshold method was then applied to generate two different threshold numbers that would later be used to label the membrane in two regions—one containing the Nafion layer and the second containing the desired element (Pt, Ir or Fe)—to determine the distribution of the specified element, Figure S11d, Supporting Information.^[29]

3. Results and Discussion

Evaluation of the samples in terms of element-specific distribution in the membrane cross-section (approach 1) and migration extent and distribution within the membrane (approach 2) was

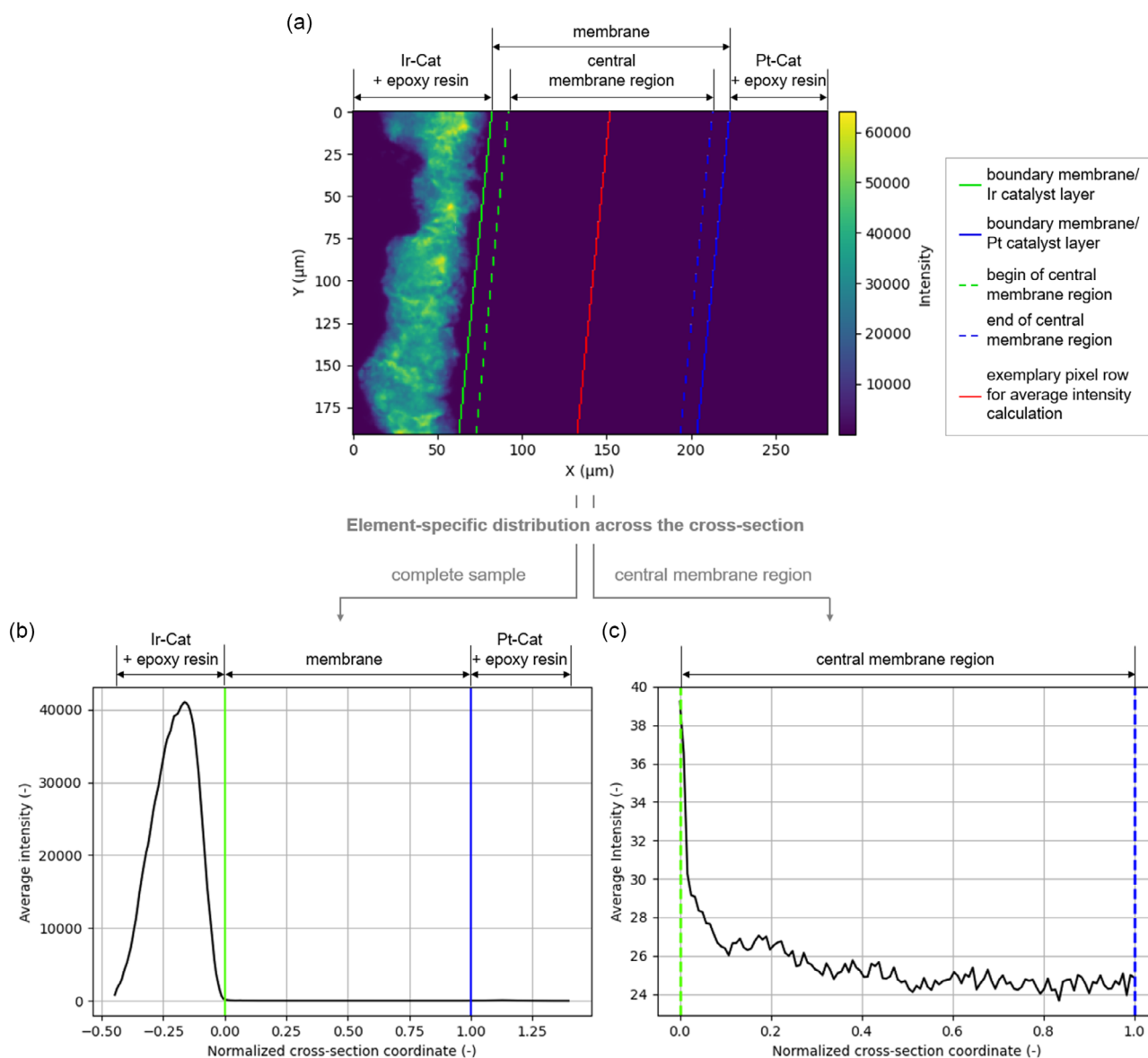


Figure 3. A methodological overview of approach 1, exemplified by the Ir XRF signal, includes: a) a two-dimensional map of the Ir XRF signal, highlighting identified characteristics and sample components (beam energy of 11.4 keV). Average intensity profiles are derived from this map, focusing on b) the sample cross-section and c) the central membrane region. The central membrane region is defined as the area excluding the outer 10 μm on each side from the specific membrane/catalyst interface. Average intensities, taken parallel to the lines indicated in the two-dimensional map, are plotted over the normalized coordinates of each respective membrane area in (b) and (c).

conducted with a focus on application scenarios in water electrolysis. These scenarios were defined to investigate the potential applications of XRF analytics in the context of PEMWE and included: 1) Migration of catalyst elements across the CCM, 2) Dissolution of PEMWE components, and 3) Contaminated water supply.

Initial short scans (10–20 min) with lower resolution provided an overview of a large area of the samples. Smaller regions of the CCM cross-section were then identified for subsequent high-resolution measurements. An essential aspect of this approach was to differentiate between high- and low-compressed areas

of the CCM cross-section (see Figure S27, Supporting Information), which occur due to the flow field structure of the PEMWE cell (see Figure S1, Supporting Information). Identical samples regions were scanned at each energy (11.7, 11.4, and 11.0 keV) for consistent examination of the same CCMs and isolation of Pt and Ir signals, where possible. Table S2, Supporting Information, shows an overview of measured samples. The measurement duration varied depending on the selected sample size, ranging between 38 and 103 min (see supplementary Table S3–S5, Supporting Information). An extended discussion of image segmentation and data analysis

(approach 2) can be found in the supporting information section, see Figure S12–S26, Supporting Information. Evaluation of the measured sulfur signal (Section S8, Supporting Information) and the sample thickness and uniformity was performed based on the absorption data (Section S9, Supporting Information). Finally, a brief discussion about oxidation states is also available in Section S10, Supporting Information.

3.1. Application Scenario I: Migration of Catalyst Elements Across the CCM

This scenario is centered around the migration of catalyst elements, Ir and Pt, into and through the membrane. Such processes have been identified as a critical factor in the degradation of PEMWE cells.^[11,12] Understanding this migration is critical to eventually improving cell durability and efficiency. The primary objective of the following scenario was to utilize XRF to assess the distribution of Ir and Pt elements within the CCM cross-section. The use of XRF aims to provide detailed insights into the migration patterns of these catalyst elements, offering a deeper understanding of their roles in the degradation process.

3.1.1. Approach 1

Ir XRF Emission Signal: **Figure 4a** depicts the average intensity values for Ir across the complete cross-sections of the samples at a beam energy of 11.4 keV. To facilitate comparison, the intensity values in the cross-section were normalized to the membrane height. In this normalization diagram, the values 0 and 1 indicate the boundaries between the membrane and the Ir catalyst layer and between the membrane and the Pt catalyst layer, respectively. The region of the anode catalyst layer is easily identifiable by high-intensity values for Ir. Conversely, a shallow level is observed within the demarcated membrane area. For pristine samples, this level is maintained across the remaining cross-section, including the cathode catalyst layer (blue and purple lines). However, increased Ir values occur within the Pt catalyst layer area for 100 h CV CCM and Fe²⁺-contaminated CCM

samples (green and orange lines). Here, the maximum average intensity values of ≈ 1973 and ≈ 2785 are significantly higher than those in the central membranous region, ≈ 45 and ≈ 30 , respectively. These results suggest that, for these two samples, Ir has already dissolved from the catalyst layer, migrated through the membrane, and eventually deposited in the area of the Pt catalyst layer again. This phenomenon has been described in earlier studies,^[11–13] making it a plausible finding.

In Figure 4b, only average intensity values across the central membrane cross-section are presented. The average Pristine CCMs exhibit a distinct pattern: relatively high intensity near the Ir catalyst layer side, rapidly diminishing to a uniform level within the membrane and toward the cathode side. In contrast, the 100 h CV CCM sample reveals significantly elevated intensity values, peaking at the membrane's center and tapering off toward the edges. Meanwhile, the Fe²⁺-contaminated CCM largely mirrors the pristine CCMs trend but with marginally lower Ir levels. These observations indicate substantial variations in Ir content among the samples, with 100 h CV CCM displaying a distinctly elevated profile compared to the others.

Pt XRF Emission Signal: **Figure 5a** presents the average intensity values of Pt XRF emission signal over the entire sample cross-section, using a beam energy of 11.7 keV. A similar qualitative progression can be observed for all samples. High average intensity values of Pt are achieved within the Pt catalyst layer, differing slightly probably due to inhomogeneous distribution of Pt particles within the different samples. Within the membrane, only very low Pt values are observed. Close to the Ir catalyst layer, there is an area of higher intensity values compared to the membrane region. At the ends of the curves, intensity values occasionally drop to low levels, indicating areas consisting solely of epoxy resin. While these trends align with expectations, the interpretation of intensity values in the region of the Ir catalyst layer requires caution due to potential interference from the presence of Ir as well.

Figure 5b focuses on the cross-section of the membrane, providing a detailed view of the element distribution. In addition to the intensity values, areas with double standard deviations are

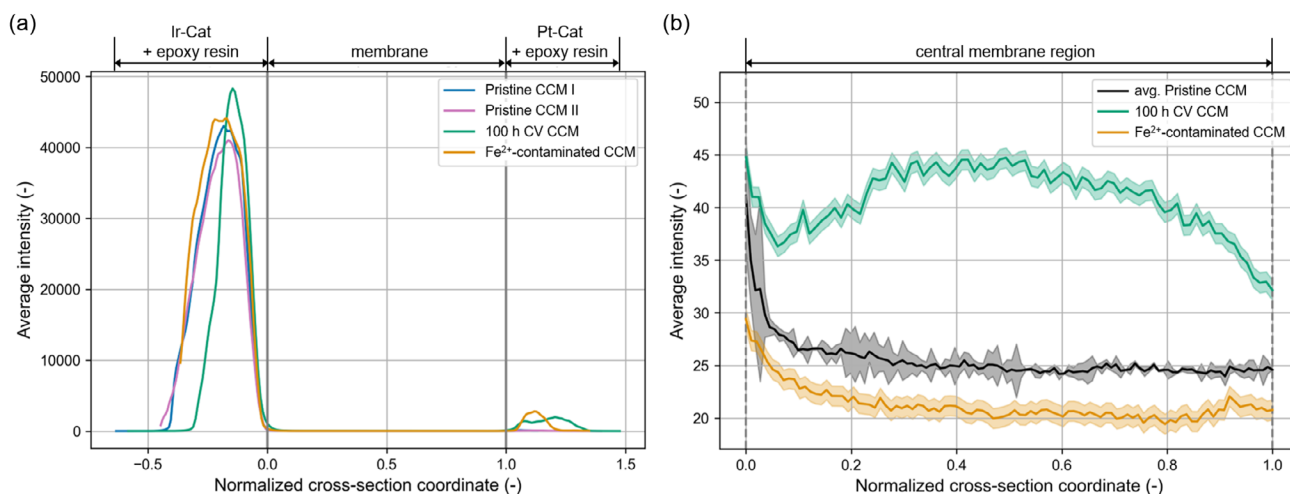


Figure 4. Average intensity profiles of Ir XRF emission signals compared across a) entire sample cross-sections and b) the central membrane regions (beam energy of 11.4 keV).

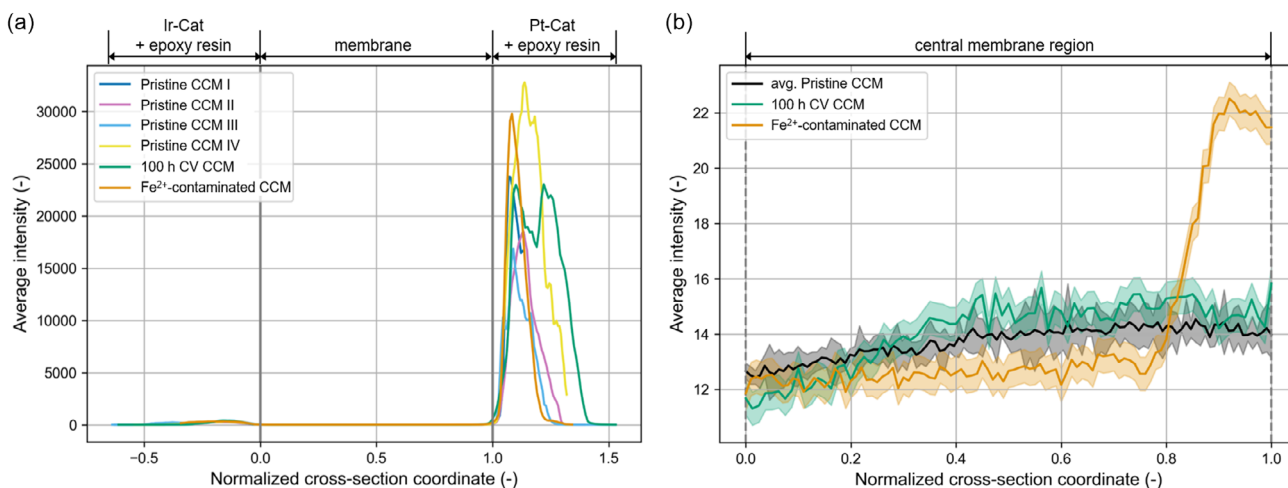


Figure 5. Average intensities of Pt XRF emission signals compared across a) entire sample cross-sections and b) the central membrane regions (beam energy of 11.7 keV).

also displayed, which are based on the measurements of the four Pristine CCMs (see Section S5.3, Supporting Information). The plotted curves show significant differences. The average Pt intensity values of the Pristine CCMs show a slight decreasing trend from the Pt catalyst layer side to the Ir catalyst layer side. The 100 h CV CCM follows this pattern, starting with the side facing the Pt catalyst layer, but decreases more in the area near the Ir catalyst layer. The Fe²⁺-contaminated CCM shows a pronounced region with high-intensity values at the boundary of the membrane on the Pt side. Apart from that, the Pt XRF emission signal over the remaining cross-section is at a slightly lower level compared to the other samples, but also with a slight decrease toward the side facing Ir catalyst layer. The pronounced Pt band observed next to the Pt catalyst layer, previously documented in both PEM fuel cells, e.g., ref. [30] and PEMWE, e.g., ref. [13], may be explained by the interruption of electrolysis operation. In the Fe²⁺-contaminated test profile, repeated cyclic voltammetry at voltages below the Nernst voltage leads to these interruptions (see Figure S3, Supporting Information). Following such interruptions, hydrogen and oxygen gases may remain in the electrode compartments, temporarily converting the electrolysis cell into a fuel cell until these gases are depleted. During this phase, platinum nanoparticles from the hydrogen electrode's active layer can dissolve into the ionomer as Pt²⁺ cations. Driven by the electric field, these cations can migrate through the membrane and are reduced back to metallic platinum by hydrogen ions, forming their own layer within the membrane.^[13] The precise localization of Pt within the membrane also opens up new possibilities for future investigations into the role and behavior of Pt interlayers, which were previously investigated mainly by electron microscopy.^[31,32]

3.1.2. Approach 2

Ir XRF Emission Signal: Figure 6a shows the Ir XRF emission signal for the pristine Nafion membrane. The apparent normal distribution indicates a uniform distribution of intensity values across the membrane structure. However, this signal is notably

diminished when compared to the corresponding signal in the 100 h CV CCM (Figure 6b). The latter demonstrates significantly higher counts for Ir XRF signal, resulting in a substantial rightward shift in the sample histogram. This shift can be attributed to the heightened density of Ir (XRF emission signal) concentrated within the Nafion membrane, compared to lower Ir signals in regions closer to the Ir catalyst layer (top), is a noteworthy observation. However, it is also feasible that sample compression within the assembled cell intensifies the Ir signal at the material's center. Consequently, this elevation of the Ir (XRF emission signal) in the central region leads to a preferential segmentation during thresholding with the Multi-Otsu method. Conversely, in the case of the Fe²⁺-contaminated CCM, shown in Figure 6c, an homogeneous distribution of Ir is observed throughout the sample. However, elevated values of the Ir signal are apparent in proximity to the catalyst layer, aligning with the anticipated behavior of Ir metal migration. The signal gradually diminishes in a smooth trend as it approaches the Pt catalyst layer, highlighting the clear difference in Ir distribution as a function of testing conditions, which apparently have an impact on metal migration.

Pt XRF Emission Signal: As shown in Figure 7a, the pristine sample exhibits a normal distribution in Pt intensity values in the membrane, similar to Ir shown above. This is again indicative of a homogeneous structural composition with minimal metal content in the membrane. Similarly, the 100 h CV CCM sample shows a normal distribution (Figure 7b). However, image labeling through the multi-Otsu method reveals a minor deviation at higher grayscale values. This leads to the observation of a discernible gradient in Pt XRF emission signal in the segmented image. The increased intensity toward the Pt catalyst layer is indicative of a minor amount of metal migration into the membrane. Noteworthy differences were observed for the Fe²⁺-contaminated CCM (Figure 7c), wherein an intense band of Pt was observed in the direct vicinity of the Pt catalyst layer. This prominent band indicates a relatively higher concentration of Pt within the membrane but is confined to the region neighboring the catalyst layer. This directly contrasts the broader

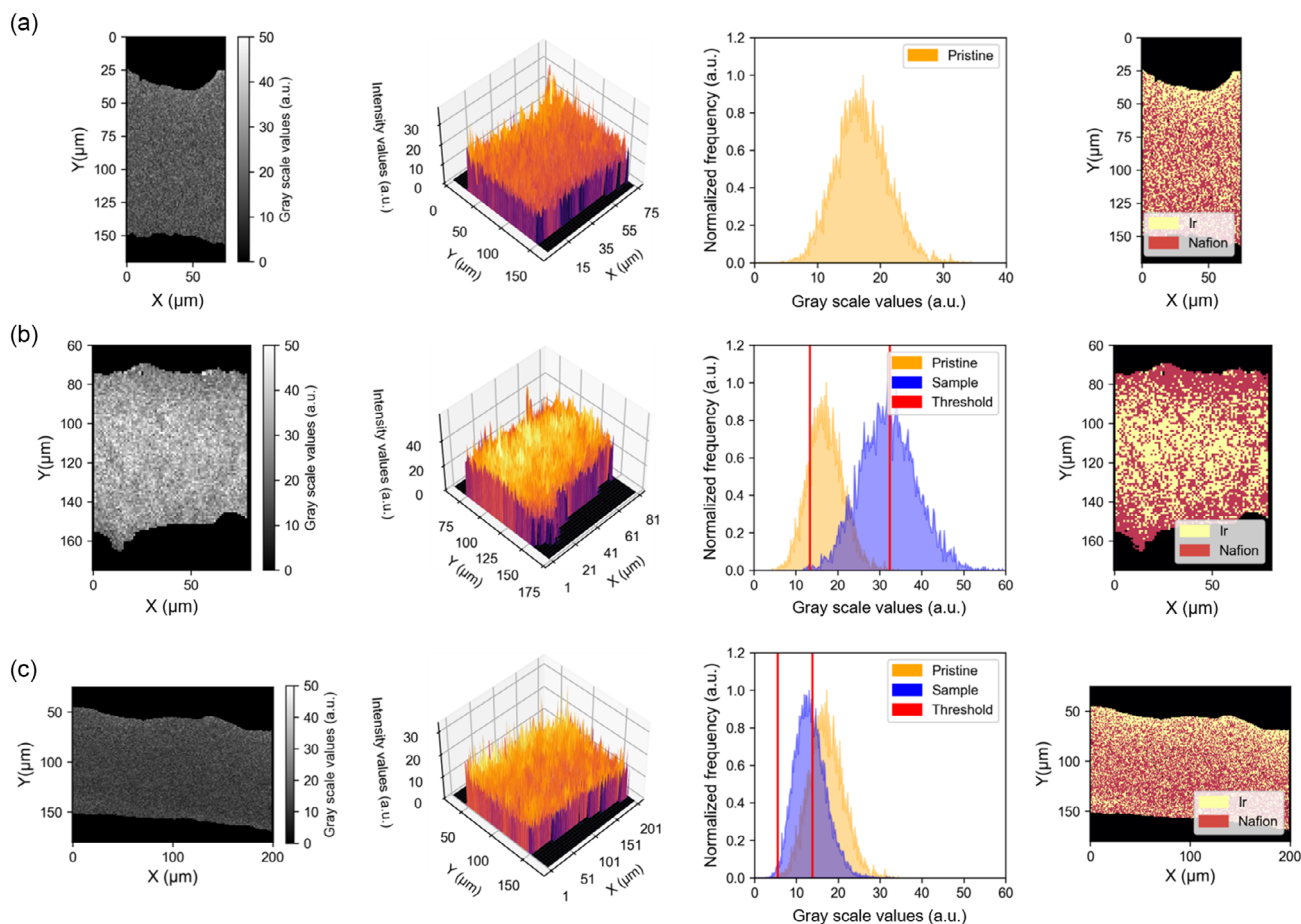


Figure 6. Ir XRF emission signal (beam energy of 11.7 keV) for multiple samples using Pristine CCM III as reference. Segmented Nafion region and corresponding histograms followed by the elemental map: a) Ir XRF emission signal—Pristine CCM III, b) Ir XRF emission signal—100 h CV CCM, and c) Ir XRF emission signal— Fe^{2+} -contaminated CCM.

distribution of Pt observed in the 100 h CV CCM, indicating again the strong influence of process conditions on metal migration behavior and catalyst ageing.

3.2. Application Scenario II: Dissolution of PEMWE Components

In this application scenario, the focus is on the degradation-induced dissolution of components within the PEMWE system, particularly emphasizing the dissolution of the Ti-PTL adjacent to the anode catalyst layer. Following up on previous studies^[15–17] that have reported the dissolution of Ti-PTL and its subsequent impact on the cathodic catalyst layer, a specific case is chosen to employ XRF analysis. The objective is to detect the Ti presence in the CCM resulting from Ti-PTL dissolution, aiming to establish a basis for future in-depth research in this area.

3.2.1. Approach 1

Ti XRF Emission Signal: Analyzing the Ti (XRF emission signal) average intensity values, the cross-section of various samples reveals that there are slightly elevated Ti XRF signals in the area

of the Ir catalyst layer compared to the membrane area, which is characterized by low average intensity values (see **Figure 8a**). This pattern is consistent across all samples analyzed. However, significant differences are noted within the Pt catalyst layer. The 100 h CV CCM and Fe^{2+} -contaminated CCM samples exhibit significantly higher Ti (XRF emission signal) values than the Pristine CCMs. In the membrane cross-section, as shown in **Figure 8b**, no significant differences in the Ti XRF signal between the samples are recognizable. These results suggest that under electrical loading conditions, Ti dissolves from the Ti-PTL adjacent to the Ir catalyst layer and migrates as Ti^{X+} ions across the membrane toward the Pt catalyst layer, driven by potential gradients, resulting in its accumulation in the cathode catalyst layer. The decomposition of Ti seems to be mostly completed before the experiments end. The evidence for this assumption is provided by the reduced Ti XRF intensities within the membrane, which closely match those observed in the pristine samples. Together with the low Ti XRF intensities on the anode side, this is probably a consequence of the formation of a titanium oxide (TiO_x) layer on the surface of the Ti-PTL as soon as the OER takes place. This TiO_x layer acts as a barrier, limiting further dissolution of Ti from the Ti-PTL. It should be noted that no conclusive data were obtained from approach 2 for Ti migration

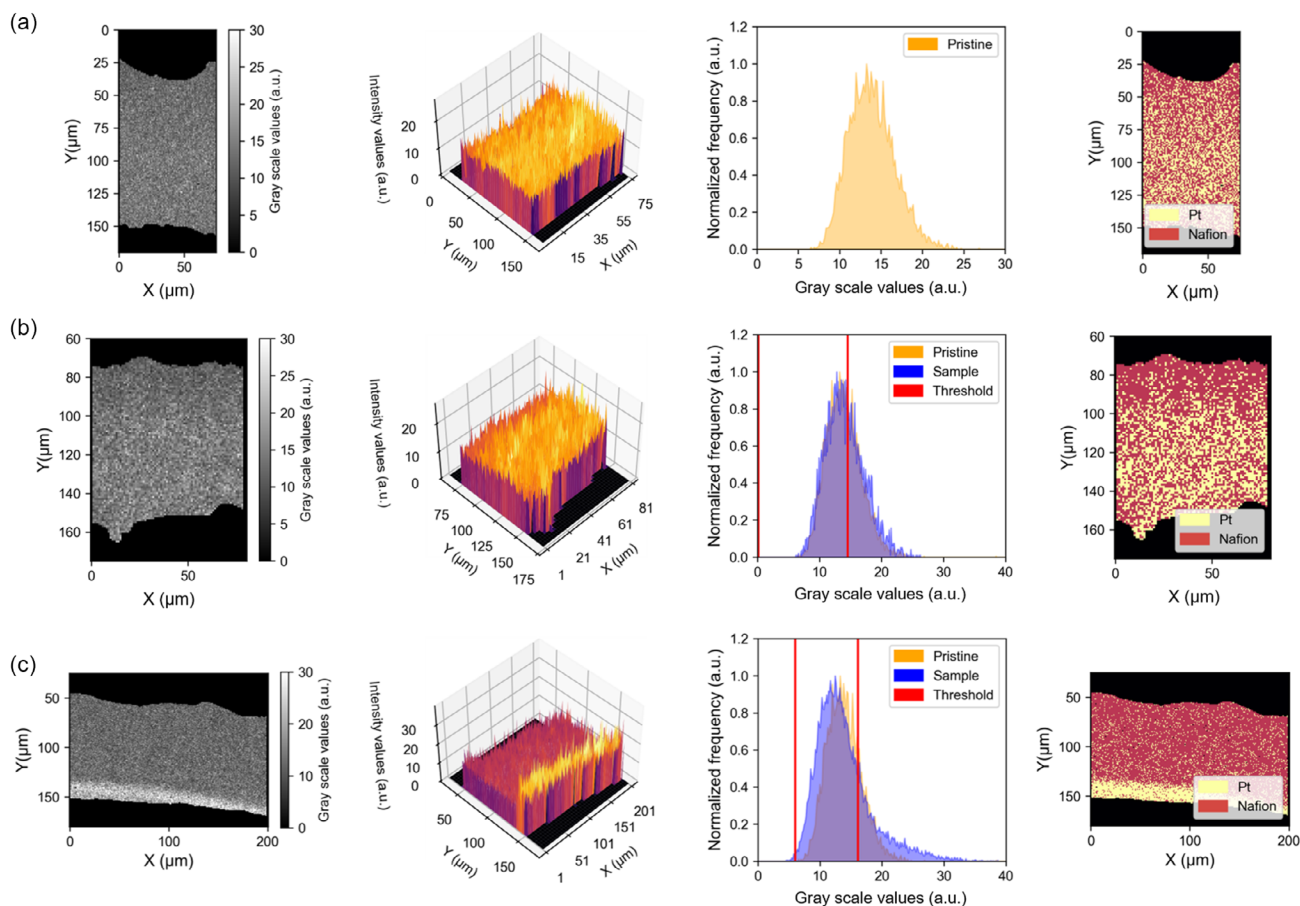


Figure 7. Pt XRF emission signal (beam energy of 11.7 keV) for multiple samples using Pristine CCM III as reference. Segmented Nafion region and corresponding histograms followed by elemental map: a) Pt XRF emission signal—Pristine CCM III, b) Pt XRF emission signal—100 h CV CCM, and c) Pt XRF emission signal— Fe^{2+} -contaminated CCM.

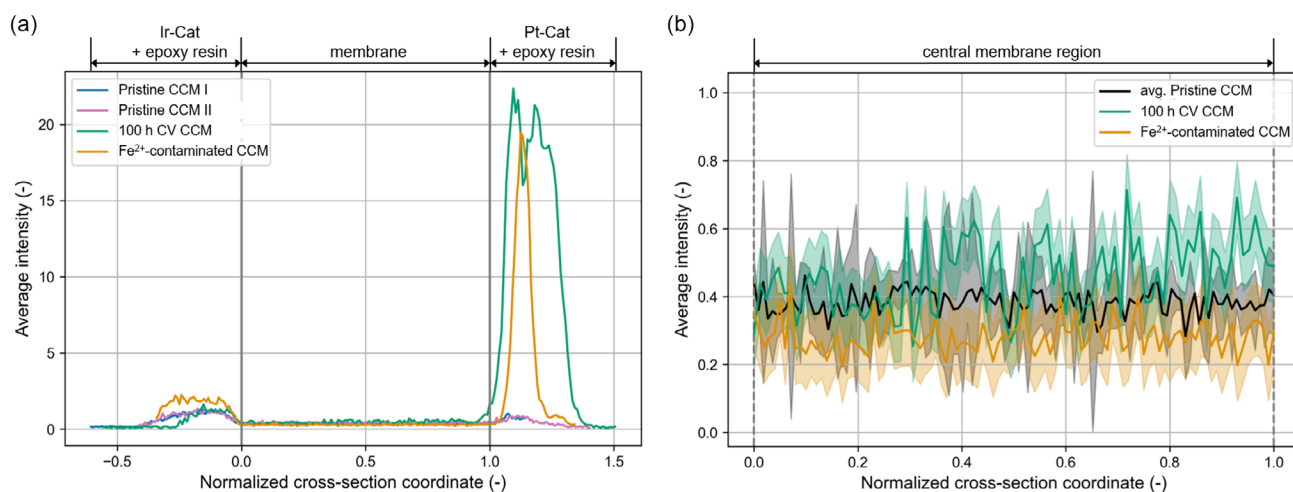


Figure 8. Average intensity profiles of Ti XRF emission signals compared across: a) entire sample cross-sections and b) the central membrane regions; (beam energy of 11.0 keV).

due to the apparent homogeneity of the samples in terms of Ti dispersion.

3.3. Application Scenario III: Contaminated Water Supply

This scenario addresses the challenge of detecting contaminants in the CCM, focusing on the membrane section. The primary concern is the potential infiltration of impurities such as iron ions into the electrolysis stack, for example, due to the dissolution of fittings containing iron or insufficient water purification processes. A specific case is chosen to demonstrate this scenario, where XRF is used to examine the extent of iron ion contamination, more specific Fe^{2+} ions, within the CCM. The analysis is designed to offer a comprehensive view of the distribution of these impurities within the membrane and to provide significant insights into their potential impact on the efficiency of the electrolysis system.

3.3.1. Approach 1

Fe XRF Emission Signal: The analysis of the sample's entire cross-section reveals a generally higher presence of iron signals in the catalyst layers compared to the membrane area, as illustrated in **Figure 9a**. For both Pristine CCMs and Fe^{2+} -contaminated CCMs, the iron signal within the membrane area remains low and constant. In contrast, 100 h CV CCM exhibits elevated Fe intensity values. This distribution pattern mirrors the Ir signal in this sample, as shown in Figure 4b. This trend can also be seen in the membrane cross-section, depicted in Figure 9b. A potential explanation for the low values in the Fe^{2+} -contaminated samples is that the Fe^{2+} ions introduced with the feed water at the anode side did not reach the CCM. Instead, they might react with oxygen on the cell's flow field and Ti-PTL surface, forming iron oxide (Fe_2O_3) and adhering to it. This is supported by the presence of significant red-brown deposits in these cell areas after testing (see Figure S35,

Supporting Information). The elevated Fe ion levels in the 100 h CV CCM might result from Fe^{3+} ions introduced into the CCM by an unknown contamination before or during the test run and, differing from the previous experiment by not forming deposits on the PTL but accumulating in the membrane instead.

However, the sensitivity of the XRF analysis must be considered. The Fe signal is 3–4 orders of magnitude lower than the signals for other elements like Ir and Pt, as clearly shown in Figure 4 and 5. Given the known loadings of 2.0 mg cm^{-2} for Ir and 1.0 mg cm^{-2} for Pt/C in the CCMs, this suggests that the Fe signal is near the probable detection limit of synchrotron XRF and is essentially insignificant. Furthermore, **Figure 10** corroborates that the distribution of the Fe content across the CCM mimics statistical noise, reinforcing the conclusion that the iron levels, though detectable, are not substantial enough to affect the CCM's performance or structural integrity significantly.

3.3.2. Approach 2

A notably lower signal was observed for the Fe (XRF emission signal), and no discernible normal distribution was identified in the case of the Pristine CCM III, as shown in Figure 10a. Upon comparing histograms for the 100 h CV CCM, an apparent overlap is evident up to 2 intensity values on the grayscale (a.u.). Subsequently, a shoulder emerges, signifying an increased Fe content within the Nafion membrane. However, after final segmentation, a uniform distribution of Fe throughout the Nafion membrane was identified, without any specific gradient attributed to it (Figure 10b). According to results shown by approach 1, Fe^{2+} also does not penetrate the Nafion layer and remains confined within the membrane, as can be seen in Figure 10c. Surprisingly, the signals from Pristine CCM III and Fe^{2+} -contaminated CCM exhibit similarity, with the latter even displaying slightly smaller nonnormalized counts, potentially stemming from nonuniformity within the sample, as a result of the sample preparation method.

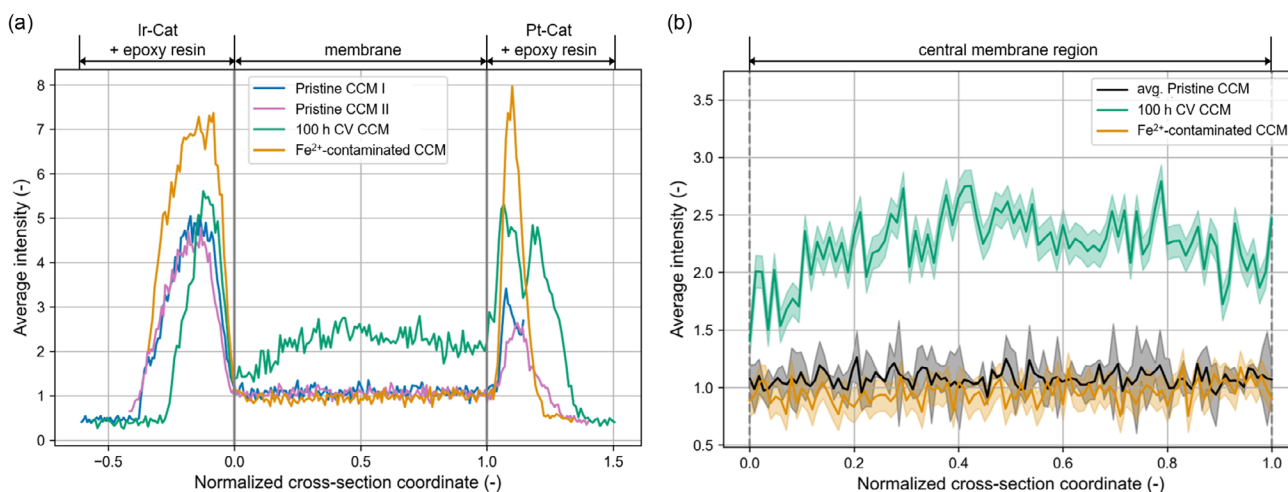


Figure 9. Average intensity profiles of Fe XRF emission signals compared across: a) entire sample cross-sections and b) the central membrane regions; (beam energy of 11.0 keV).

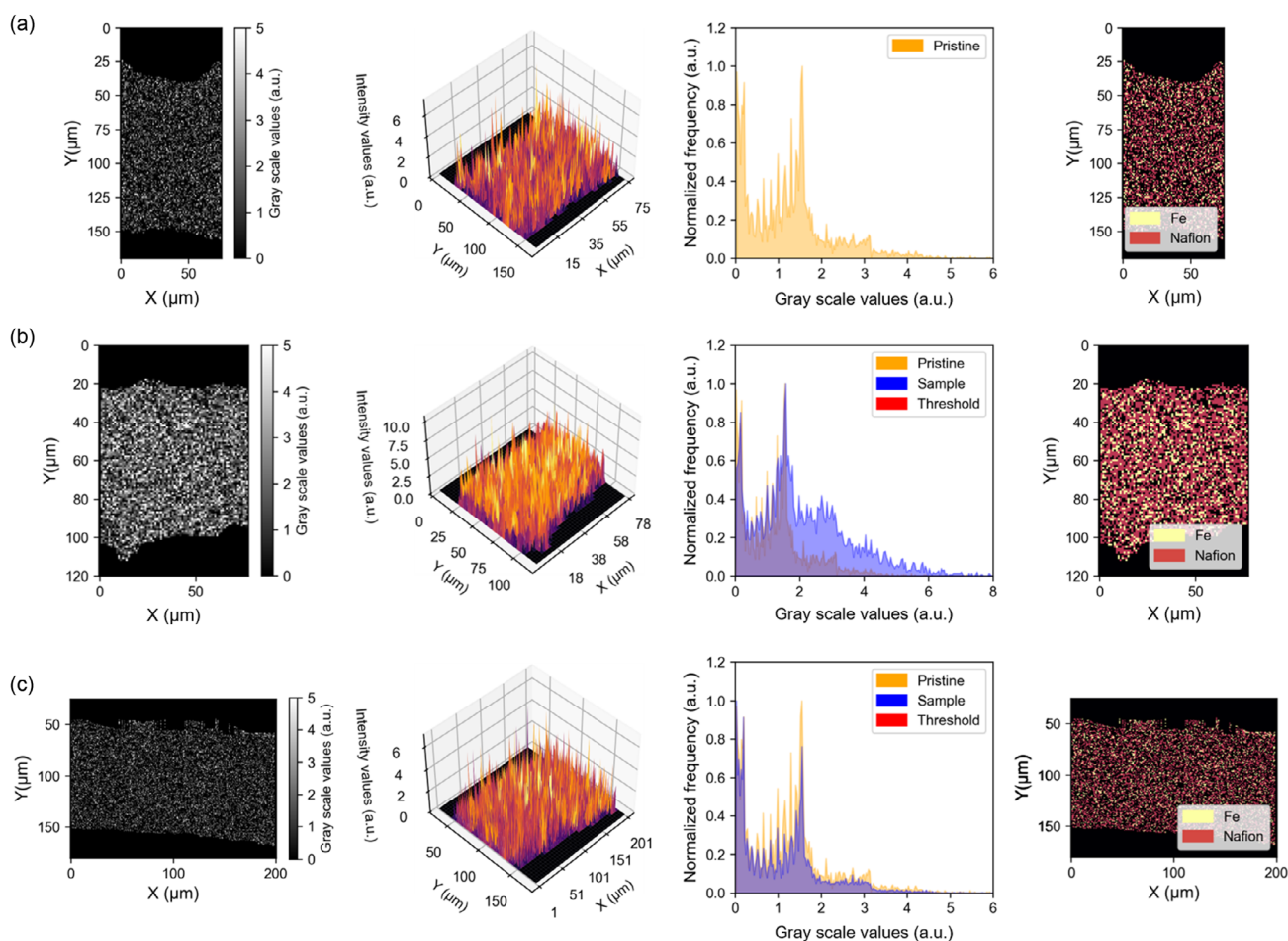


Figure 10. Fe XRF emission signal (beam energy of 11.7 keV) for multiple samples using Pristine CCM III as reference. Segmented Nafion region and corresponding histograms followed by the elemental map: a) Fe XRF emission signal—Pristine CCM III, b) Fe XRF emission signal—100 h CV CCM, and c) Fe XRF emission signal—Fe²⁺-contaminated CCM.

3.4. 2D XRF Mapping as Method for Investigating the Metal Distribution

The discussion points surrounding the use of XRF for mapping metal distribution reveal several important considerations. First, XRF offers high throughput capabilities, allowing for the observation of metals at a specified resolution while conducting rapid scans over large samples, typically on the order of millimeters. This capacity enables detailed mapping of element distribution along the samples, making it well-suited for the proposed application scenarios. However, the method's effectiveness is contingent upon various factors, including the use of different energies for optimal differentiation between elements. While this approach aids in distinguishing between elements, such as Pt, some interference, particularly with the Pt signal at 11.7 keV, may pose challenges.

Moreover, the intensity signals of both highly and minimally compressed samples exhibit minimal changes, complicating differentiation. Quantification also emerges as a challenge, necessitating improvements in sample preparation, for example, preparing samples of uniform thickness, and the use of appropriate standards to enhance accuracy. Additionally, the sulfur

signal, crucial for certain analyses, is susceptible to disturbance by variations in sample thickness and cannot be reliably compared to assess sample thickness by XRF due to self-absorption artifacts. Moreover, regarding absorbance signals for thickness evaluation and quantification, the limitation of this methodology relies on tracing maps only for the Nafion membrane region and can be limited by differences in density over time due to metal migration. Finally, an interface issue arises, as the tail of the XRF beam limits the evaluation of the interface between the membrane and catalyst layers. This limitation may be attributed to the size and shape of the focused beam, emphasizing the need for further investigation and potential methodological refinements to address these challenges effectively.

4. Conclusion and Outlook

The results of the study demonstrate that XRF is an effective method for assessing the elemental distribution across the PEMWE CCMs in various application scenarios and sample types. The investigation involved different stressed CCMs, including pristine samples serving as baselines, a CCM stressed

at 2 V for around 100 h, and a CCM in which the feed water was contaminated with Fe²⁺ ions. XRF measurements, conducted at PSI, utilized three distinct energies (11.7, 11.4, 11.0 keV) to differentiate between Pt, Ir, and additional elements such as Ti, Fe, and Cl. Two approaches were developed to evaluate element-specific image signals, providing both a comprehensive overview of the sample and a more detailed analysis through segmentation and imaging techniques.

In examining three application scenarios, significant insights emerged: Ir: analysis revealed the highest Ir content in the membrane for the 100 h CV CCM sample, with a pronounced peak at the membrane's center. Both Pristine and Fe²⁺-contaminated CCMs exhibited a decreasing Ir trend from the anode to the cathode side. However, the Fe²⁺-contaminated CCM displayed a left-shifted histogram compared to the Pristine CCM III, indicating decreased Ir intensity, likely due to washout. Pt: both approaches demonstrated a gradient from the cathode to the anode side in Pristine and 100 h CV CCM samples. Conversely, the Fe²⁺-contaminated CCM exhibited a distinct Pt band adjacent to the Pt catalyst layer. Ti: approach 1 revealed Ti signal decomposition in the cathode catalyst layer but no significant differences in membrane intensity across samples subjected to electrical load. This suggests that most Ti migration occurred within the first 100 h, with TiO_x formation potentially inhibiting further migration. Fe: the Fe signals were generally lower and exhibited nonnormal distribution (statistical noise). Interestingly, Fe²⁺-contaminated CCM showed a distribution similar to Pristine CCM, suggesting Fe²⁺ did not penetrate the sample. These observations underline the utility of XRF in evaluating elemental distribution within PEMWE membranes under various conditions, offering valuable insights into system stability and the potential impact on performance.

Additionally, the study provides several perspectives. In view of the open questions remaining after the experiments, further investigations are needed to clarify remaining uncertainties and to refine our understanding of elemental distribution within PEMWE membranes. It is noteworthy that sample preparation plays a fundamental role in facilitating further analysis, and sample preparation procedures are crucial for obtaining reliable and meaningful results. As the estimation of the sample thickness absorption signal has shown, an upgrade of the current method should be developed to enhance the accuracy and precision of elemental distribution measurements. Quantitative assessments are achievable only with samples of similar thickness and the availability of standards for calibration purposes. In situ measurements present a promising avenue for precisely observing metal migration along the membrane. By utilizing a PEMWE single cell and aging it over time with a proper setup, more robust 2D XRF mapping experiments could be conducted. Further methods should be explored to improve the clarity of the sulfur signal evaluation. The study did not consider membrane areas close to the catalyst layers (10 μm thick); although in literature significant quantities of catalyst elements may be detected in these areas.

Supporting Information

Supporting Information is available from the Wiley Online Library or from the author.

Acknowledgements

A.R. and L.A.d.C. contributed equally to this work. The Swiss Light Source (SLS) is acknowledged for providing beam time under the accepted proposal (20221749). Gratitude is extended to the microXAS beamline team for their assistance during measurements and data processing. L.A.d.C. and T.S. acknowledge support from the German Federal Ministry of Education and Research, Röntgen-Ångström Cluster (RAC) project 13K22VKA. The Institute of Electric Power Systems at Leibniz University Hannover acknowledges the support from the HoKaWe project (BMBF 03EI3029B) and PowerMEM project (BMBF 03EW0012B). Acknowledgment is given to the H2Wind project (BMBF 03HY301H), within the context of which the full cell measurements with Fe²⁺-contaminated sample were carried out, and to the HyThroughGen project (BMBF 03HY108C), from which the rest of the full cell measurements originate. Appreciation is also extended to Dr. Florian Bittner from the Institute of Plastics and Circular Economy (IKK) at Leibniz University Hannover for the provision of essential support, equipment, and materials for sample preparation.

Conflict of Interest

The authors declare no conflict of interest.

Data Availability Statement

The data that support the findings of this study are openly available in RADAR4KIT at <https://doi.org/10.35097/CtiKQoyOgLCNsOBP>, <https://doi.org/10.35097/cjrGdnJmzvVZRJZ>, and <https://doi.org/10.35097/UhRarunqHJGutUVx>.

Keywords

catalyst-coated membranes, material stability, metal migration, proton exchange membrane water electrolysis, X-Ray fluorescence

Received: February 14, 2024

Revised: May 15, 2024

Published online:

- [1] A. Makhsoos, M. Kandidayeni, B. G. Pollet, L. Boulon, *Int. J. Hydrogen Energy* **2023**, *48*, 15341.
- [2] C. V. Pham, D. Escalera-López, K. Mayrhofer, S. Cherevko, S. Thiele, *Adv. Energy Mater.* **2021**, *11*, 2101998.
- [3] Q. Wang, Y. Cheng, H. B. Tao, Y. Liu, X. Ma, D.-S. Li, H. B. Yang, B. Liu, *Angew. Chem. Int. Ed.* **2023**, *62*, e202216645.
- [4] F.-Y. Chen, Z.-Y. Wu, Z. Adler, H. Wang, *Joule* **2021**, *5*, 1704.
- [5] S. Cherevko, *Curr. Opin. Electrochem.* **2018**, *8*, 118.
- [6] Q. Feng, X.-Z. Yuan, G. Liu, B. Wei, Z. Zhang, H. Li, H. Wang, *J. Power Sources* **2017**, *366*, 33.
- [7] M. Suermann, B. Bensmann, R. Hanke-Rauschenbach, *J. Electrochem. Soc.* **2019**, *166*, F645.
- [8] M. J. Burch, K. A. Lewinski, M. I. Buckett, S. Luopa, F. Sun, E. J. Olson, A. J. Steinbach, *J. Power Sources* **2021**, *500*, 229978.
- [9] G. Papakonstantinou, G. Algara-Siller, D. Teschner, T. Vidaković-Koch, R. Schlögl, K. Sundmacher, *Appl. Energy* **2020**, *280*, 115911.
- [10] S. Zhao, A. Stocks, B. Rasimick, K. More, H. Xu, *J. Electrochem. Soc.* **2018**, *165*, F82.
- [11] M. Milosevic, T. Böhm, A. Körner, M. Bierling, L. Winkelmann, K. Ehelebe, A. Hutzler, M. Suermann, S. Thiele, S. Cherevko, *ACS Energy Lett.* **2023**, *8*, 2682.

- [12] H. Yu, L. Bonville, J. Jankovic, R. Maric, *Appl. Catal. B: Environ.* **2020**, 260, 118194.
- [13] S. A. Grigoriev, D. G. Bessarabov, V. N. Fateev, *Russ. J. Electrochem.* **2017**, 53, 318.
- [14] S. Czioska, A. Boubnov, D. Escalera-López, J. Geppert, A. Zagalskaya, P. Röse, E. Saraçi, V. Alexandrov, U. Krewer, S. Cherevko, J.-D. Grunwaldt, *ACS Catal.* **2021**, 11, 10043.
- [15] C. Rakousky, U. Reimer, K. Wippermann, M. Carmo, W. Lueke, D. Stolten, *J. Power Sources* **2016**, 326, 120.
- [16] C. Rakousky, U. Reimer, K. Wippermann, S. Kuhri, M. Carmo, W. Lueke, D. Stolten, *J. Power Sources* **2017**, 342, 38.
- [17] S. Garbe, J. Futter, A. Agarwal, M. Tarik, A. A. Mularczyk, T. J. Schmidt, L. Gubler, *J. Electrochem. Soc.* **2021**, 168, 044515.
- [18] H. Becker, J. Murawski, D. V. Shinde, I. E. L. Stephens, G. Hinds, G. Smith, *Sustainable Energy Fuels* **2023**, 7, 1565.
- [19] J. Garrevoet, B. Vekemans, S. Bauters, A. Demey, L. Vincze, *Anal. Chem.* **2015**, 87, 6544.
- [20] L. Mino, E. Borfecchia, J. Segura-Ruiz, C. Giannini, G. Martinez-Criado, C. Lamberti, *Rev. Mod. Phys.* **2018**, 90, 025007.
- [21] S. Das, R. Pashminehazar, S. Sharma, S. Weber, T. L. Sheppard, *Chem. Ing. Tech.* **2022**, 94, 1591.
- [22] S. Kalirai, U. Boesenberg, G. Falkenberg, F. Meirer, B. M. Weckhuysen, *ChemCatChem* **2015**, 7, 3674.
- [23] S. R. Bare, M. E. Charochak, S. D. Kelly, B. Lai, J. Wang, Y.-C. K. Chen-Wiegart, *ChemCatChem* **2014**, 6, 1427.
- [24] J. Ruiz-Martínez, A. M. Beale, U. Deka, M. G. O'Brien, P. D. Quinn, J. F. W. Mosselmans, B. M. Weckhuysen, *Angew. Chem. Int. Ed.* **2013**, 52, 5983.
- [25] I. Carlomagno, M. Antonelli, G. Aquilanti, P. Bellutti, G. Bertuccio, G. Borghi, G. Cautero, D. Cirrincione, G. de Giudici, F. Ficorella, M. Gandola, D. Giuressi, D. Medas, F. Mele, R. H. Menk, L. Olivi, G. Orzan, A. Picciotto, F. Podda, A. Rachevski, I. Rashevskaya, L. Stebel, A. Vacchi, G. Zampa, N. Zampa, N. Zorzi, C. Meneghini, *J. Synchrotron Radiat.* **2021**, 28, 1811.
- [26] N. Bukowiecki, M. Hill, R. Gehrig, C. N. Zwicky, P. Lienemann, F. Hegedüs, G. Falkenberg, E. Weingartner, U. Baltensperger, *Environ. Sci. Technol.* **2005**, 39, 5754.
- [27] T. Lickert, S. Fischer, J. L. Young, S. Klose, I. Franzetti, D. Hahn, Z. Kang, M. Shviro, F. Scheepers, M. Carmo, T. Smolinka, G. Bender, S. Metz, *Appl. Energy* **2023**, 352, 121898.
- [28] V. Solé, E. Papillon, M. Cotte, P. Walter, J. Susini, *Spectrochim. Acta, Part B* **2007**, 62, 63.
- [29] D.-Y. Huang, C.-H. Wang, *Pattern Recognit. Lett.* **2009**, 30, 275.
- [30] S. G. Rinaldo, J. Stumper, M. Eikerling, *J. Phys. Chem. C* **2010**, 114, 5773.
- [31] D. Abbas, A. Martin, P. Trinke, M. Bierling, B. Bensmann, S. Thiele, R. Hanke-Rauschenbach, T. Böhm, *J. Electrochem. Soc.* **2022**, 169, 124514.
- [32] Z. Zhang, Z. Han, A. Testino, L. Gubler, *J. Electrochem. Soc.* **2022**, 169, 104501.